Supporting Information

Layer-by-layer assembly based heterointerfaces for modulating electronic properties of $Ti_3C_2T_x$ MXene

Keshab Karmakar,[a,#] Prakash Sarkar,[a,#] Jenifar Sultana,[a] Narendra Kurra,[c] K. D. M Rao,*[a,b]

[a]*School of Applied & Interdisciplinary Sciences, Indian Association for the Cultivation of Science, 2A & 2B Raja S. C. Mullick Road, Jadavpur, Kolkata 700032, India. E-mail: mallik2arjun@gmail.com (K. D. M. R.).*
[b]*Technical Research Centre, Indian Association for the Cultivation of Science, 2A & 2B Raja S. C. Mullick Road, Jadavpur, Kolkata 700032, India. E-mail: trckdmr@iacs.res.in (K. D. M. R).*
[c]*Department of Chemistry, Indian Institute of Technology Hyderabad, Kandi-502284, Sangareddy Telangana, India.*

Table of Content

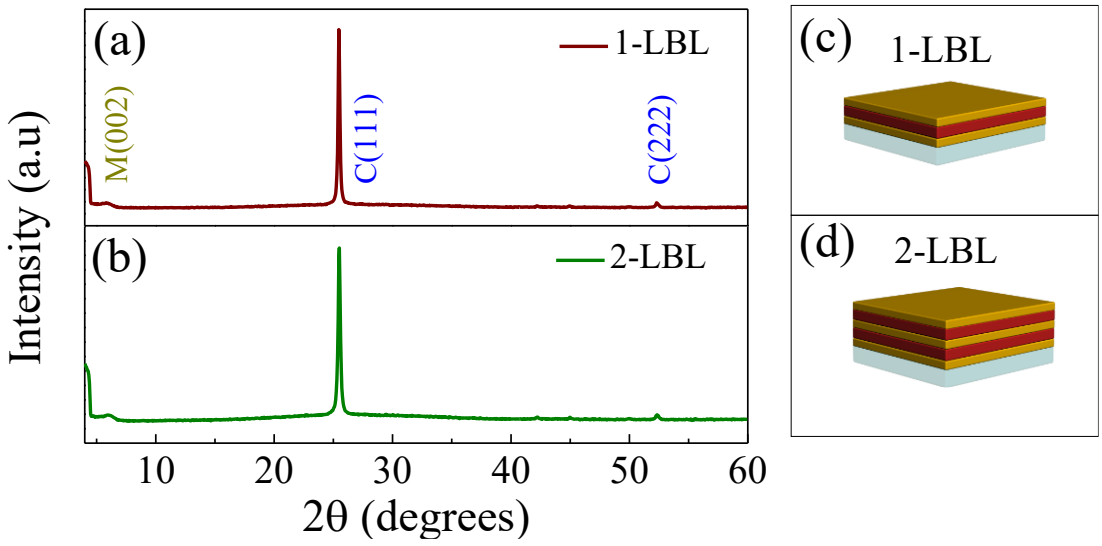

Figure S1: XRD patterns of (a) 1-LBL, and (b) 2-LBL assembly, respectively. Dark yellow and blue color index represents the peak corresponding to $Ti_3C_2T_x$ MXene (M) and CuI (C), respectively; schematic diagram of the (c) 1-LBL and (d) 2-LBL, respectively.

The XRD patterns of 1-LBL and 2-LBL assembly are depicted in Figure S1(a-b), which demonstrates the existence of $Ti_3C_2T_x$ MXene and CuI nanoparticles. The schematic of 1-LBL and 2-LBL assembly is presented in Figures S1c & S1d to reveal the stacking of $Ti_3C_2T_x$ MXene and CuI nanoparticle layers.

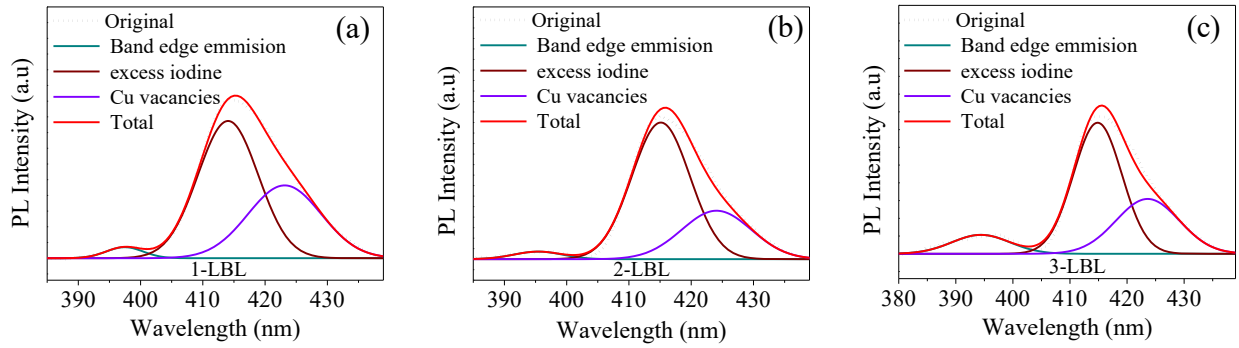

Figure S2: Photoluminescence spectra and deconvoluted peaks of (a) 1-LBL, (b) 2-LBL, (c) 3-LBL assemblies, respectively. Dark cyan, wine, and violet color curves represent band edge-related emission, excess iodine, Cu vacancies as indexed in the inset of each figure. Black dotted and red curves represent raw data and cumulative peak fitting results of PL.

The Photoluminescence (PL) spectra of 1-LBL, 2-LBL, and 3-LBL assembly are shown in Figure S2(a-c), when excited with 350 nm wavelength of light. All the PL spectra are

deconvoluted into three peaks corresponding to band edge emission, excess Iodine, and Cu vacancy. The corresponding peak positions are tabulated in Table S1.

Table S1: Deconvoluted PL Peak positions of CuI thin film, 1-LBL, 2-LBL, and 3-LBL assembly.

Peak Assigned for	**CuI** (nm)	**1-LBL** (nm)	**2-LBL** (nm)	**3-LBL** (nm)
Band edge emission	398	397	396	394
Excess iodine	416	414	414	414
Cu vacancy	425	423	423	423

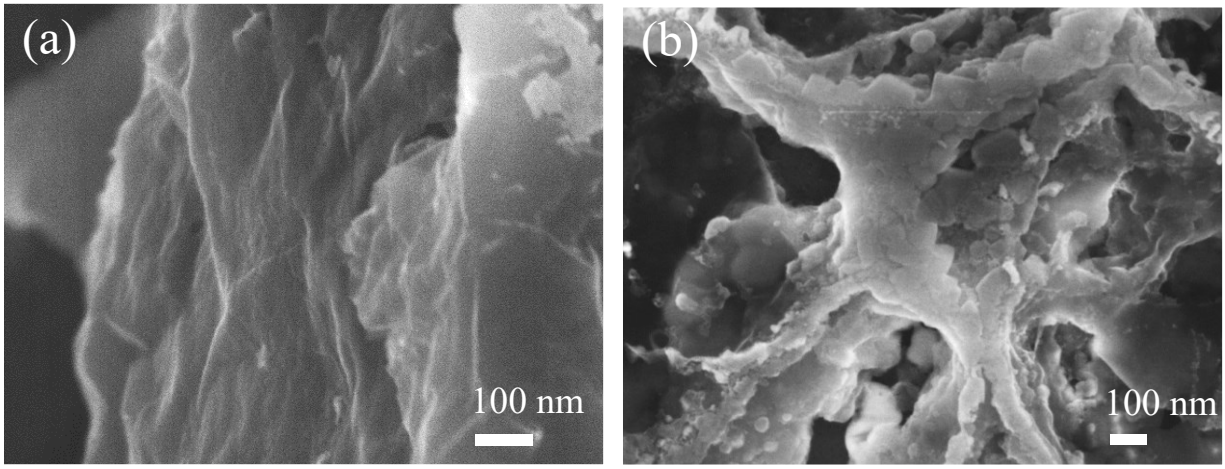

Figure S3: a) Magnified view of FESEM micrographs of (a) $Ti_3C_2T_x$ MXene thin film, and (b) 3-LBL assembly.

Figure S3a depicts the magnified view of the marked in the main manuscript Figure 3b, which reveals stacked nanosheets edges in $Ti_3C_2T_x$ MXene thin-film. The magnified view (see Figure S3b) of the 3-LBL assembly is marked in the main manuscript Figure 3h, which demonstrates edge capping of MXene nanosheets with CuI nanoparticles.

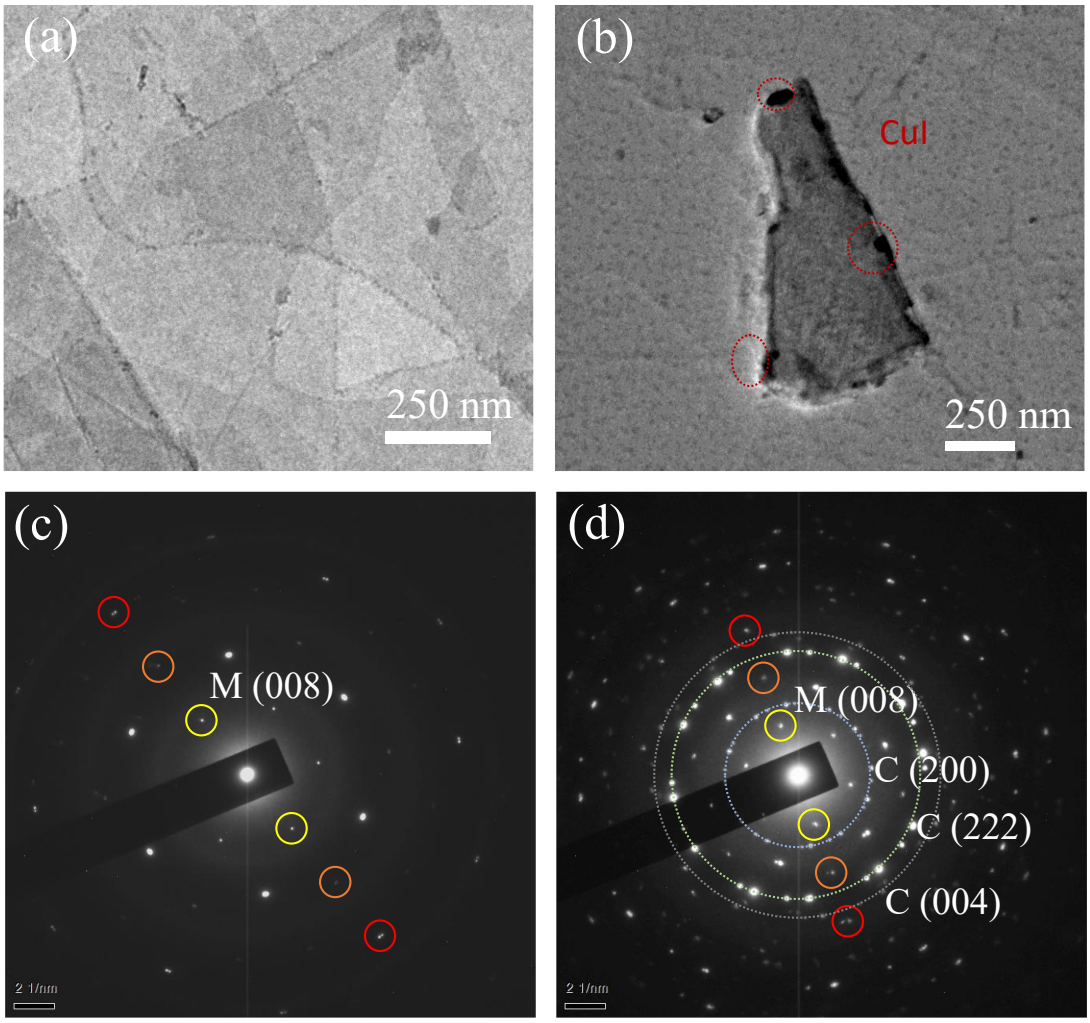

Figure S4: TEM images of (a) $Ti_3C_2T_x$ MXene nanosheets and (b) $Ti_3C_2T_x$ MXene nanosheets/CuI nanoparticles (3-LBL assembly), selective portions are highlighted by red circles to represent CuI nanoparticles. SAED patterns of (c) $Ti_3C_2T_x$ MXene and (d) LBL assembly.

The TEM image of as-prepared $Ti_3C_2T_x$ MXene is displayed in Figure S4a, demonstrating the staking of nanosheets. The TEM image of CuI nanoparticles coated $Ti_3C_2T_x$ MXene (3-LBL) is illustrated in Figure S4b, which suggests the engulfing of CuI nanoparticles (deep dark contrast) at the edges of the MXene nanosheet. $Ti_3C_2T_x$ MXene SAED patterns in Figure S4c revealed crystalline behavior containing (00*l*) plane spots. The diffraction spots of LBL heterointerfacial assembly in Figure S4d manifested the polycrystalline nature of CuI nanoparticles along with $Ti_3C_2T_x$ MXene (00*l*) plane spots. Moreover, the $Ti_3C_2T_x$ MXene crystalline behavior is intact

even after the fabrication of LBL heterointerfacial assembly with CuI nanoparticles. The SAED pattern discloses the increased interlayer spacing in $Ti_3C_2T_x$ MXene (00*l*) planes of LBL assembly, which is consistent with the estimated *d*-spacing from XRD patterns Figure 1c.

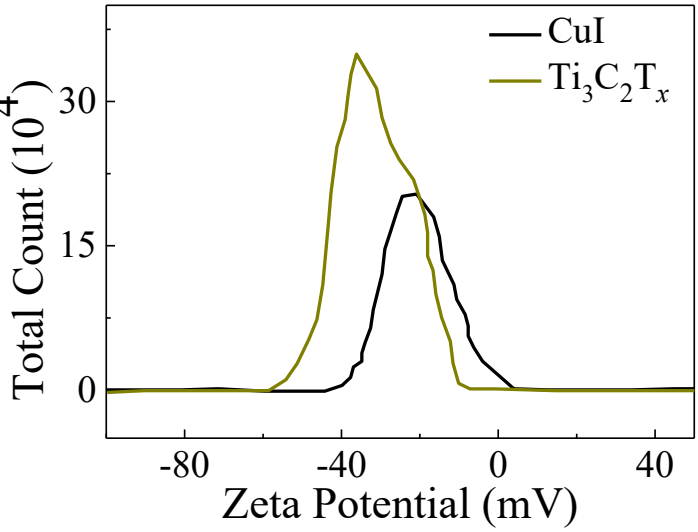

Figure S5: Zeta potential of colloidal $Ti_3C_2T_x$ MXene dispersion and CuI solution in water.

As shown in Figure S5a, the Zeta potential of CuI nanoparticles and $Ti_3C_2T_x$ MXene nanosheets are estimated to be -35.9 and -20.7 mV, respectively. Previously, the $Ti_3C_2T_x$ MXene are reported to have -29 mV zeta potential attributed to the negative surface charge.[1] Therefore, the intrinsic surface charge difference between CuI nanoparticles and $Ti_3C_2T_x$ MXene instigates the electrostatic interactions, which is the driving force for the fabrication of heterointerfacial assembly.

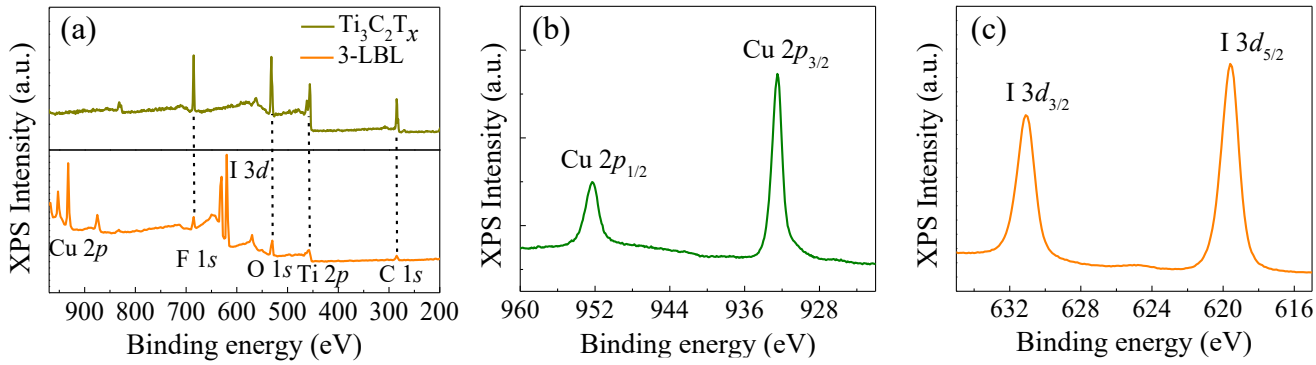

Figure S6: (a) XPS survey scan of $Ti_3C_2T_x$ MXene thin film and 3-LBL assembly. Core-level spectra of (b) Cu 2*p*, and (c) I 3*d* for the 3-LBL assembly.

All the elements corresponding to $Ti_3C_2T_x$ MXene thin film (Ti, C, F, O) and 3-LBL assembly (Ti, C, F, O, I, Cu) are revealed in the XPS surface survey scan as shown in Figure S6a. The 3-LBL assembly core-level spectra of Cu 2*p* consist of doublet (see Figure S6b, Cu $2p_{1/2}$ at 952.29 and Cu$2p_{3/2}$ at 932.50 eV), which suggests '+1' oxidation state of Cu, and the absence of any satellite peak confirms the existence of the copper Iodide phase.[2] The peak positions of I $3d_{3/2}$ at 631.08 eV, and I $3d_{5/2}$ at 619.58 eV manifest '-1' oxidation state of iodine as shown in core-level spectra (see Figure S6c). The red-shift in the core level peaks of I $3d_{3/2}$ (631.08 eV) and I $3d_{5/2}$, (619.58 eV) in 3-LBL assembly compared to pure Iodine peaks 631.5 and 620.3 eV, endorse the bonding between $Ti_3C_2T_x$ MXene and Iodine.

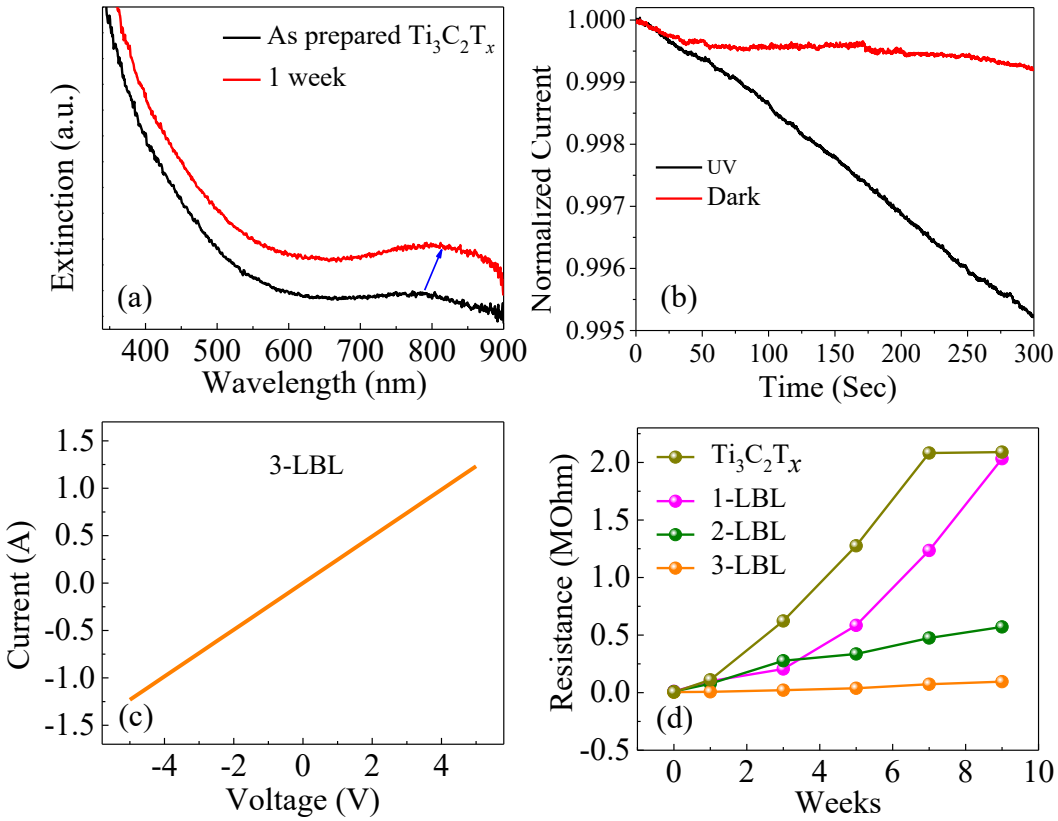

Figure S7: (a) UV-vis extinction spectra of the $Ti_3C_2T_x$ MXene recorded before and after ambient atmosphere for one week. Blue arrow indicates plasmonic peak shift to higher wavelength attributed to the Ti oxidation state change in $Ti_3C_2T_x$ MXene thin film. (b) Normalized current decay behavior of $Ti_3C_2T_x$ MXene in dark and UV light illumination conditions. (c) I-V characteristics of 3-LBL assembly at room temperature. (d) Resistance of 1-LBL, 2-LBL, 3-LBL assembly, and MXene thin film, while exposed to the ambient atmosphere for two months.

The $Ti_3C_2T_x$ MXene plasmonic peak is depicted in UV-vis extinction spectra as shown in Figure S7a, a shift in plasmonic peak is observed upon one-week exposer to the ambient atmosphere which indicates the oxidation of $Ti_3C_2T_x$ MXene. We also investigated the current decaying behavior of the $Ti_3C_2T_x$ MXene thin-film under constant UV light illumination and compared it with the dark condition. Figure S4b shows the current decay behavior up to 300 seconds which demonstrates the $Ti_3C_2T_x$ MXene thin-film current decays under UV light illumination, whereas, the dark condition reveals a steady-state current. The UV light illumination along with ambient O_2, and humidity accelerates the current decay owing to adsorbed O_2 or H_2O molecules on the $Ti_3C_2T_x$ MXene surface. (Chertopalov *et al. ACS Nano* 2018, 12, 6109−6116) Therefore, UV light exposure rapidly deteriorates the conductivity of $Ti_3C_2T_x$ MXene attributed to the formation of sub-oxidized species. Figure S7c presents the I-V characteristics of the 3-LBL assembly which demonstrates linear ohmic behavior. Furthermore, the linear resistance of the $Ti_3C_2T_x$ MXene and LBL assemblies are demonstrated in Figure S7d, where the samples are exposed to ambient conditions over two months and the periodic measurements are noted. Among all the samples $Ti_3C_2T_x$ MXene manifested maximum change in linear resistance and the 3-LBL assembly exhibited almost constant linear resistance for two months. Therefore, the 3-LBL assembly revealed the excellent oxidation stability of $Ti_3C_2T_x$ MXene heterointerfaces in atmospheric environmental conditions.

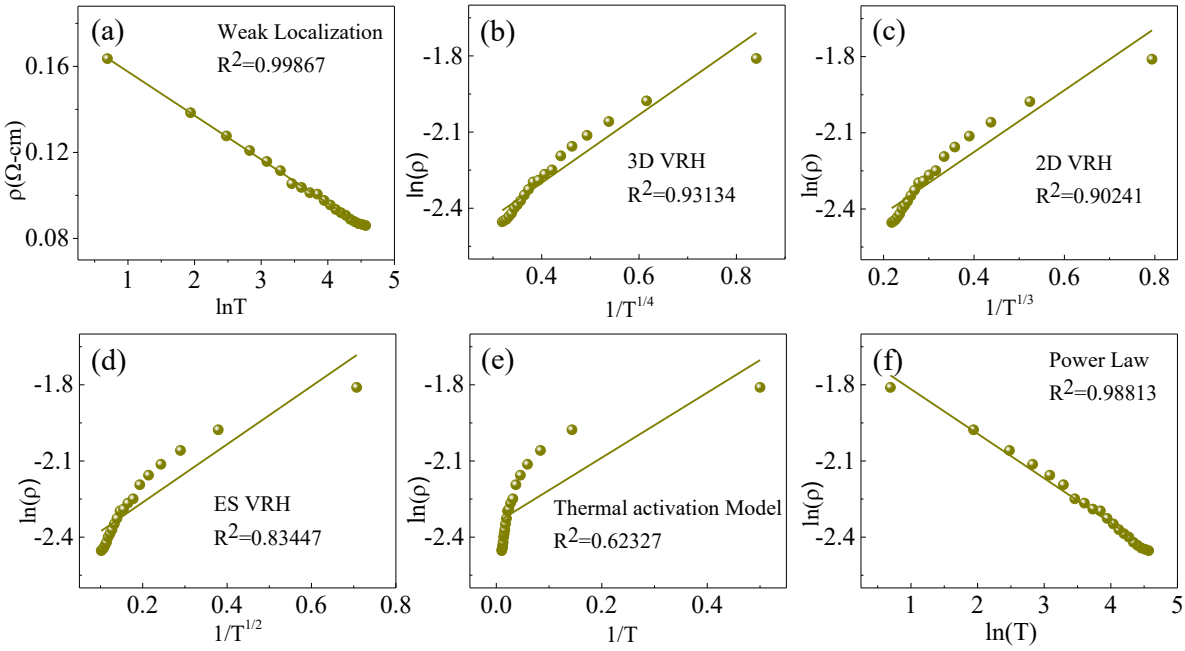

Figure S8: The $Ti_3C_2T_x$ MXene thin film low-temperature resistivity data fitting over the temperature range from 2 to 100 K, corresponding to (a) weak localization, (b) 3D VRH, (c) 2D VRH, (d) E-S VRH, (e) thermal activation, and (f) power law models.

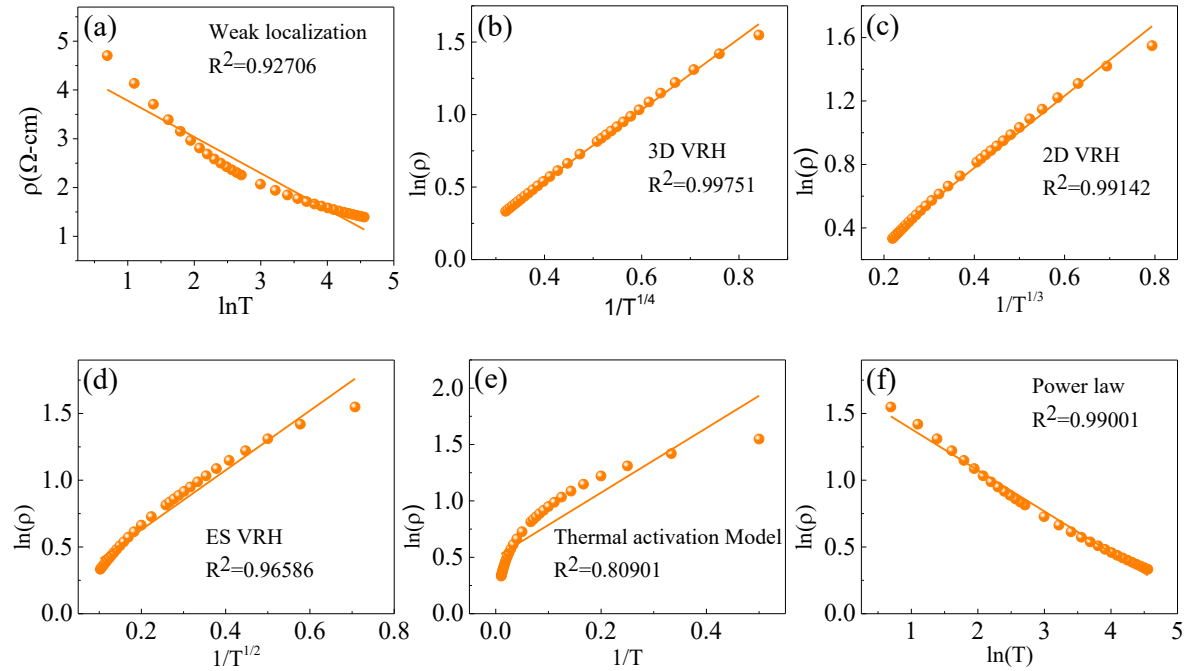

Figure S9: The 3-LBL assembly low-temperature resistivity data fitting over the temperature range from 2 to 100 K, corresponding to (a) weak localization, (b) 3D VRH, (c) 2D VRH, (d) E-S VRH, (e) thermal activation, and (f) power-law models.

Electrical transport measurements of the $Ti_3C_2T_x$ MXene thin film and 3-LBL assembly are performed at low temperature. Figures S8-S9 demonstrate the resistivity data from 2 to 100 K temperature and six electrical transport models are tried for the fitting of the experimental data. Following are the transport mechanisms and corresponding resistivity equations[3-7]

(a) weak localization model for which $\rho \sim \ln(T)$,

(b) 3D variable range hopping for which $\rho \sim \exp(T_0/T)^{1/4}$,

(c) 2D variable range hopping for which $\rho \sim \exp(T_0/T)^{1/3}$,

(d) Efros- Shklovskii variable range hopping for which $\rho \sim \exp(T_0/T)$,

(e) thermally activated model for which $\rho \sim \exp(E_A/kT)$,

(f) power law for which $\rho \sim AT^p$,

Where ρ = resistivity, T_0 = initial temperature, T = actual temperature, E_A = activation energy, k = Boltzmann constant, and A = arbitrary constant.

Figure S8(a-f) and Figure S9(a-f) represent all the six electrical transport models fitting for $Ti_3C_2T_x$ MXene thin film and 3-LBL assembly resistivity data. In the case of $Ti_3C_2T_x$ MXene, the weak localization model in Figure S8a is the best fit with a maximum value of the fitting parameter (R^2). The weak localization-based electrical transport is typically observed in 2D materials due to the electron backscattering at the boundaries of nanosheets. However, 3-LBL assembly demonstrated a 3D variable range hopping-based electrical conduction mechanism (see Figure S9b) attributed to the charge transfer at $Ti_3C_2T_x$ MXene/CuI nanoparticles heterointerfaces and enables the hopping process to allow the seamless movement of electrons in 3D dimensions.

References:

1. H. Tang, H. Feng, H. Wang, X. Wan and J. Liang. Highly Conducting MXene–Silver Nanowire Transparent Electrodes for Flexible Organic Solar Cells. *ACS Appl. Mater. Interfaces*, 2019, **11**, 25330–25337.

2. Vasquez, R. P. CuI by XPS. *Surf. Sci. Spectra* **1993**, *2*, 149–154.

3. D. Yu, C. Wang, B. L. Wehrenberg, P. Guyot-Sionnest, Variable Range Hopping Conduction in Semiconductor Nanocrystal Solids. *Phys. Rev. Lett.* 2004, 92, 216802.

4. G. Bergmann. Quantitative analysis of weak localization in thin Mg films by magnetoresistance measurements *Phys. Rev. B* 1982, 25, 2937-2939.

5. G. Bergmann. Weak localization in thin films: a time-of-flight experiment with conduction electrons. *Phys. Rep.* 1984, 107, 1-58.

6. T. Abraham*,* C. Bansal*,* J. T. T. Kumaran*, and* A. Chatterjee. Efros-Shklovskii variable range hopping transport in nanocluster metallic films. *Journal of Applied Physics*, 2012, **111**, 104318.

7. Anasori, B.; Shi, C.; Moon, E. J.; Xie, Y.; Voigt, C. A.; Kent, P. R. C.; May, S. J.; Billinge, S. J. L.; Barsoum, M. W.; Gogotsi, Y. Control of Electronic Properties of 2D Carbides (MXenes) by Manipulating Their Transition Metal Layers. *Nanoscale Horizons* **2016**, *1*, 227–234.